

***In vivo* high-contrast imaging of deep posterior eye by 1- μ m swept source optical coherence tomography and scattering optical coherence angiography**

**Yoshiaki Yasuno^{*1}, Youngjoo Hong¹, Shuichi Makita¹,
Masahiro Yamanari¹, Masahiro Akiba², Masahiro Miura^{1,3} and
Toyohiko Yatagai⁴**

¹Computational Optics Group in the University of Tsukuba, Tsukuba, Ibaraki, Japan
and Computational Optics and Ophthalmology Group, Tsukuba, Ibaraki, Japan

²Yamagata Promotional Organization for Industrial Technology, Yamagata, Yamagata, Japan

³Department of Ophthalmology, Tokyo Medical University, Shinjuku, Tokyo, Japan

⁴Institute of Applied Physics, University of Tsukuba, Tsukuba, Ibaraki, Japan

*yasuno@optlab2.bk.tsukuba.ac.jp

<http://optics.bk.tsukuba.ac.jp/COG/>

Abstract: Retinal, choroidal and scleral imaging by using swept-source optical coherence tomography (SS-OCT) with a 1- μ m band probe light, and high-contrast and three-dimensional (3D) imaging of the choroidal vasculature are presented. This SS-OCT has a measurement speed of 28,000 A-lines/s, a depth resolution of 10.4 μ m in tissue, and a sensitivity of 99.3 dB. Owing to the high penetration of the 1- μ m probe light and the high sensitivity of the system, the *in vivo* sclera of a healthy volunteer can be observed. A software-based algorithm of scattering optical coherence angiography (S-OCA) is developed for the high-contrast and 3D imaging of the choroidal vessels. The S-OCA is used to visualize the 3D choroidal vasculature of the *in vivo* human macula and the optic nerve head. Comparisons of S-OCA with several other angiography techniques including Doppler OCA, Doppler OCT, fluorescein angiography, and indocyanine green angiography are also presented.

© 2007 Optical Society of America

OCIS codes: (170.4470) Ophthalmology; (170.4500) Optical coherence tomography; (170.3890) Medical optics instrumentation; (100.5010) Pattern recognition and feature extraction; (100.6890) Three-dimensional image processing; (100.2650) Fringe analysis; (110.6880) Three-dimensional image acquisition; (110.4500) Optical coherence tomography.

References and links

1. A. F. Fercher, C. K. Hitzenberger, G. Kamp, and S. Y. El-Zaiat, "Measurement of intraocular distances by back-scattering spectral interferometry," *Opt. Commun.* **117**, 43–48 (1995).
2. G. Häusler and M. W. Lindner, "Coherence radar" and "spectral radar" —New tools for dermatological diagnosis," *J. Biomed. Opt.* **3** (1998).
3. D. Huang, E. A. Swanson, W. G. S. C. P. Lin, J. S. Schuman, W. Chang, T. F. M. R. Hee, K. Gregory, C. A. Puliafito, and J. G. Fujimoto, "Optical coherence tomography," *Science* **254**, 1178–1181 (1991).
4. J. Welzel, "Optical coherence tomography in dermatology: a review," *Skin Res. Technol.* **7**, 1–9 (2001).
5. Y. Hori, Y. Yasuno, S. Sakai, M. Matsumoto, T. Sugawara, V. Madjarova, M. Yamanari, S. Makita, T. Yasui, T. Araki, M. Itoh, and T. Yatagai, "Automatic characterization and segmentation of human

- skin using three-dimensional optical coherence tomography," *Opt. Exp.* **14**, 1862–1877 (2006), URL <http://www.opticsinfobase.org/abstract.cfm?URI=oe-14-5-1862>.
6. G. J. Tearney, I.-K. Jang, and B. E. Bouma, "Optical coherence tomography for imaging the vulnerable plaque," *J. Biomed. Opt.* **11**, 021,002 (2006).
 7. T. Xie, M. Zeidel, and Y. Pan, "Detection of tumorigenesis in urinary bladder with optical coherence tomography: optical characterization of morphological changes," *Opt. Exp.* **10**, 1431–1443 (2002), URL <http://www.opticsinfobase.org/abstract.cfm?URI=oe-10-24-1431>.
 8. B. Colston, U. Sathyam, L. DaSilva, M. Everett, P. Stroeve, and L. Otis, "Dental OCT," *Opt. Exp.* **3**, 230–238 (1998), URL <http://www.opticsinfobase.org/abstract.cfm?URI=oe-3-6-230>.
 9. V. D. Madjarova, Y. Yasuno, S. Makita, Y. Hori, J.-B. Voeffray, M. Itoh, T. Yatagai, M. Tamura, and T. Nanbu, "Investigations of soft and hard tissues in oral cavity by spectral domain optical coherence tomography," *Proc. SPIE, Coherence Domain Optical Methods and Optical Coherence Tomography in Biomedicine X* **6079**, 60,790N (2006).
 10. J. S. Schuman, C. A. Puliafito, and J. G. Fujimoto, eds., *Optical Coherence Tomography of Ocular Diseases*, 2nd ed. (Slack Incorporated, 2004).
 11. M. Wojtkowski, V. Srinivasan, J. G. Fujimoto, T. Ko, J. S. Schuman, A. Kowalczyk, and J. S. Duker, "Three-dimensional retinal imaging with high-speed ultrahigh-resolution optical coherence tomography," *Ophthalmology* **112**, 1734–1746 (2005).
 12. T. C. Chen, B. Cense, M. C. Pierce, N. Nassif, B. H. Park, S. H. Yun, B. R. White, B. E. Bouma, G. J. Tearney, and J. F. de Boer, "Spectral domain optical coherence tomography: ultra-high speed, ultra-high resolution ophthalmic imaging," *Arch. Ophthalmol.* **123**, 1715–1720 (2005).
 13. U. Schmidt-Erfurth, R. A. Leitgeb, S. Michels, B. Povazay, S. Sacu, B. Hermann, C. Ahlers, H. Sattmann, C. Scholda, A. F. Fercher, and W. Drexler, "Three-dimensional ultrahigh-resolution optical coherence tomography of macular diseases," *Invest. Ophthalmol. Vis. Sci.* **46**.
 14. S. Alam, R. J. Zawadzki, S. Choi, C. Gerth, S. S. Park, L. Morse, and J. S. Werner, "Clinical application of rapid serial fourier-domain optical coherence tomography for macular imaging," *Ophthalmology* **113**, 1425–1431 (2006).
 15. V. J. Srinivasan, M. Wojtkowski, A. J. Witkin, J. S. Duker, T. H. Ko, M. Carvalho, J. S. Schuman, A. Kowalczyk, and J. G. Fujimoto, "High-definition and 3-dimensional imaging of macular pathologies with high-speed ultrahigh-resolution optical coherence tomography," *Ophthalmology* **113**, 2054.e1–2054.14 (2006).
 16. M. Hangai, Y. Ojima, N. Gotoh, R. Inoue, Y. Yasuno, S. Makita, M. Yamanari, T. Yatagai, M. Kita, and N. Yoshimura, "Three-dimensional Imaging of Macular Holes with High-speed Optical Coherence Tomography," *Ophthalmology* **114**, 763–773 (2007).
 17. H. Lim, J. F. de Boer, B. H. Park, E. C. Lee, R. Yelin, and S. H. Yun, "Optical frequency domain imaging with a rapidly swept laser in the 815–870 nm range," *Opt. Exp.* **14**, 5937–5944 (2006), URL <http://www.opticsinfobase.org/abstract.cfm?URI=oe-14-13-5937>.
 18. H. Lim, M. Mujat, C. Kerbage, E. C. Lee, Y. Chen, T. C. Chen, and J. F. de Boer, "High-speed imaging of human retina in vivo with swept-source optical coherence tomography," *Opt. Exp.* **14**, 12,902–12,908 (2006), URL <http://www.opticsinfobase.org/abstract.cfm?URI=oe-14-26-12902>.
 19. V. Srinivasan, R. Huber, I. Gorczynska, J. Fujimoto, J. Jiang, P. Reisen, and A. Cable, "High-speed, high resolution Optical Coherence Tomography retinal imaging with a frequency-swept laser at 850 nm," *Opt. Lett.* **32**, 361–363 (2007).
 20. B. Cense, "Optical coherence tomography for retinal imaging," Ph.D. thesis, Twente University (2005).
 21. T. Chen, M. Mujat, B. Park, and J. de Boer, "Spectral Domain Optical Coherence Tomography Imaging of Glaucoma Patients," *Invest. Ophthalmol. Vis. Sci., E-Abstract* **47**, 2695 (2006).
 22. J. D. Gass, *Stereoscopic atlas of macular diseases*, 4th ed. (Mosby, 1997).
 23. L. A. Yannuzzi, K. T. Rohrer, L. J. Tindel, R. S. Sobel, M. A. Costanza, W. Shields, and E. Zang, "Fluorescein angiography complication survey," *Ophthalmology* **93**, 611–617 (1986).
 24. M. Hope-Ross, L. A. Yannuzzi, E. S. Gragoudas, D. R. Guyer, J. S. Slakter, J. A. Sorenson, S. Krupsky, D. A. Orlock, and C. A. Puliafito, "Adverse reactions due to indocyanine green," *Ophthalmology* **101**, 529–533 (1994).
 25. Z. Chen, T. E. Milner, D. Dave, and J. S. Nelson, "Optical Doppler tomographic imaging of fluid flow velocity in highly scattering media," *Opt. Lett.* **22**, 64–66 (1997).
 26. S. Yazdanfar, A. M. Rollins, and J. A. Izatt, "In vivo imaging of human retinal flow dynamics by color Doppler optical coherence tomography," *Arch. Ophthalmol.* **121**, 235–239 (2003).
 27. R. A. Leitgeb, L. Schmetterer, W. Drexler, A. F. Fercher, R. J. Zawadzki, and T. Bajraszewski, "Real-time assessment of retinal blood flow with ultrafast acquisition by color Doppler Fourier domain optical coherence tomography," *Opt. Exp.* **11**, 3116–3121 (2003), URL <http://www.opticsinfobase.org/abstract.cfm?id=78206>.
 28. B. R. White, M. C. Pierce, N. Nassif, B. Cense, B. H. Park, G. J. Tearney, B. E. Bouma, T. C. Chen, and J. F. de Boer, "In vivo dynamic human retinal blood flow imaging using ultrahigh-speed spectral domain optical coherence tomography," *Opt. Exp.* **11**, 3490–3497 (2003), URL <http://www.opticsinfobase.org/abstract.cfm?URI=oe-11-25-3490>.
 29. S. Makita, Y. Hong, M. Yamanari, T. Yatagai, and Y. Yasuno, "Optical coherence angiography," *Opt. Exp.* **14**,

- 7821–7840 (2006), URL <http://www.opticsinfobase.org/abstract.cfm?URI=oe-14-17-7821>.
30. S. Radhakrishnan, A. Rollins, J. Roth, S. Y. V. Westphal, D. Bardenstein, and J. Izatt, "Real-time optical coherence tomography of the anterior segment at 1310 nm," *Arch. Ophthalmol.* **119**, 1179–1185 (2001).
 31. Y. Yasuno, V. D. Madjarova, S. Makita, M. Akiba, A. Morosawa, C. Chong, T. Sakai, K. Chan, M. Itoh, and T. Yatagai, "Three-dimensional and high-speed swept-source optical coherence tomography for in vivo investigation of human anterior eye segments," *Opt. Exp.* **13**, 10,652–10,664 (2005), URL <http://www.opticsinfobase.org/abstract.cfm?URI=oe-13-26-10652>.
 32. M. Sarunic, B. Applegate, S. Asrani, and J. Izatt, "Quadrature Projection Full Range High Speed Fourier Domain Optical Coherence Tomography," *Invest. Ophthalmol. Vis. Sci., E-Abstract* **47**, 2928 (2006).
 33. M. V. Sarunic, B. E. Applegate, and J. A. Izatt, "Real-time quadrature projection complex conjugate resolved Fourier domain optical coherence tomography," *Opt. Lett.* **31**, 2426–2428 (2006).
 34. G. M. Hale and M. R. Querry, "Optical constants of water in the 200-nm to 200- μ m wavelength region," *Appl. Opt.* **12**, 555–563 (1973).
 35. Y. Wang, Z. C. J. Nelson, B. Reiser, R. Chuck, and R. Windeler, "Optimal wavelength for ultrahigh-resolution optical coherence tomography," *Opt. Exp.* **11**, 1411–1417 (2003), URL <http://www.opticsinfobase.org/abstract.cfm?URI=oe-11-12-1411>.
 36. A. Unterhuber, B. Povazay, B. Hermann, H. Sattmann, A. Chavez-Pirson, and W. Drexler, "In vivo retinal optical coherence tomography at 1040 nm — enhanced penetration into the choroid," *Opt. Exp.* **13**, 3252–3258 (2005), URL <http://www.opticsinfobase.org/abstract.cfm?URI=oe-13-9-3252>.
 37. T. Mitsui, "Dynamic Range of Optical Reflectometry with Spectral Interferometry," *Jpn. J. Appl. Phys.* **38**, 6133–6137 (1999).
 38. R. A. Leitgeb, C. K. Hitzenberger, and A. F. Fercher, "Performance of fourier domain vs. time domain optical coherence tomography," *Opt. Exp.* **11**, 889–894 (2003), URL <http://www.opticsinfobase.org/abstract.cfm?URI=oe-11-8-889>.
 39. J. F. de Boer, B. Cense, B. H. Park, M. C. Pierce, G. J. Tearney, and B. E. Bouma, "Improved signal-to-noise ratio in spectral-domain compared with time-domain optical coherence tomography," *Opt. Lett.* **28**, 2067–2069 (2003).
 40. M. A. Choma, M. V. Sarunic, C. Yang, and J. A. Izatt, "Sensitivity advantage of swept source and Fourier domain optical coherence tomography," *Opt. Exp.* **11**, 2183–2189 (2003), URL <http://www.opticsinfobase.org/abstract.cfm?URI=oe-11-18-2183>.
 41. M. Wojtkowski, T. Bajraszewski, P. Targowski, and A. Kowalczyk, "Real-time in vivo imaging by high-speed spectral optical coherence tomography," *Opt. Lett.* **28**, 1745 (2003).
 42. N. A. Nassif, B. Cense, B. H. Park, M. C. Pierce, S. H. Yun, B. E. Bouma, G. J. Tearney, T. C. Chen, and J. F. de Boer, "In vivo high-resolution video-rate spectral-domain optical coherence tomography of the human retina and optic nerve," *Opt. Exp.* **12**, 367–376 (2004), URL <http://www.opticsinfobase.org/abstract.cfm?URI=oe-12-3-367>.
 43. S. H. Yun, G. J. Tearney, J. F. de Boer, N. Ifimia, and B. E. Bouma, "High-speed optical frequency-domain imaging," *Opt. Exp.* **11**, 2953–2963 (2003), URL <http://www.opticsinfobase.org/abstract.cfm?URI=oe-11-22-2953>.
 44. S. H. Yun, G. J. Tearney, J. F. de Boer, and B. E. Bouma, "Motion artifacts in optical coherence tomography with frequency-domain ranging," *Opt. Exp.* **12**, 2977–2998 (2004), URL <http://www.opticsinfobase.org/abstract.cfm?URI=oe-12-13-2977>.
 45. W. Y. Oh, S. H. Yun, G. J. Tearney, and B. E. Bouma, "115 kHz tuning repetition rate ultrahigh-speed wavelength-swept semiconductor laser," *Opt. Lett.* **30**, 3159–3161 (2005).
 46. R. Huber, M. Wojtkowski, and J. G. Fujimoto, "Fourier Domain Mode Locking (FDML): A new laser operating regime and applications for optical coherence tomography," *Opt. Exp.* **14**, 3225–3237 (2006), URL <http://www.opticsinfobase.org/abstract.cfm?id=89307>.
 47. R. Huber, D. C. Adler, and J. G. Fujimoto, "Buffered Fourier domain mode locking: Unidirectional swept laser sources for optical coherence tomography imaging at 370,000 lines/s," *Opt. Lett.* **31**, 2975–2977 (2006).
 48. J. Zhang, Q. Wang, B. Rao, Z. Chen, and K. Hsu, "Swept laser source at 1 μ m for Fourier domain optical coherence tomography," *Appl. Phys. Lett.* **89**, 073,901 (2006).
 49. E. C. Lee, J. F. de Boer, M. Mujat, H. Lim, and S. H. Yun, "In vivo optical frequency domain imaging of human retina and choroid," *Opt. Exp.* **14**, 4403–4411 (2006), URL <http://www.opticsinfobase.org/abstract.cfm?URI=oe-14-10-4403>.
 50. B. Vakoc, S. Yun, J. de Boer, G. Tearney, and B. Bouma, "Phase-Resolved Optical Frequency Domain Imaging," *Opt. Exp.* **13**, 5483–5493 (2005), URL <http://www.opticsinfobase.org/abstract.cfm?id=84914>.
 51. J. Zhang and Z. Chen, "In vivo blood flow imaging by a swept laser source based Fourier domain optical Doppler tomography," *Opt. Exp.* **13**, 7449–7457 (2005), URL <http://www.opticsinfobase.org/abstract.cfm?URI=oe-13-19-7449>.
 52. M. Pircher, E. Götzinger, O. Findl, S. Michels, W. Geitzenauer, C. Leydolt, U. Schmidt-Erfurth, and C. K. Hitzenberger, "Human macula investigated in vivo with polarization-sensitive optical coherence tomography," *Invest. Ophthalmol. Vis. Sci.* **47**, 5487–5494 (2006).
 53. A. N. S. institute, *American National Standard for the Safe Use of Lasers ANSI Z136.1-2000* (American National

Standards institute, New York, 2000).

54. M. Wojtkowski, R. Leitgeb, A. Kowalczyk, T. Bajraszewski, and A. F. Fercher, "In vivo human retinal imaging by Fourier domain optical coherence tomography," *J. Biomed. Opt.* **7**, 457–463 (2002).
55. R. Tripathi, N. Nassif, J. S. Nelson, B. H. Park, and J. F. de Boer, "Spectral shaping for non-Gaussian source spectra in optical coherence tomography," *Opt. Lett.* **27**, 406–408 (2002).
56. R. A. Leitgeb, W. Drexler, A. Unterhuber, B. Hermann, T. Bajraszewski, T. Le, A. Stingl, and A. F. Fercher, "Ultrahigh resolution Fourier domain optical coherence tomography," *Opt. Exp.* **12**, 2156–2165 (2004),
57. M. Wojtkowski, V. J. Srinivasan, T. H. Ko, J. G. Fujimoto, A. Kowalczyk, and J. S. Duker, "Ultrahigh-resolution, high-speed, Fourier domain optical coherence tomography and methods for dispersion compensation," *Opt. Exp.* **12**, 2404–2422 (2004), URL <http://www.opticsinfobase.org/abstract.cfm?URI=oe-12-11-2404>.
58. B. Cense, N. A. Nassif, T. C. Chen, M. C. Pierce, S.-H. Yun, B. H. Park, B. E. Bouma, G. J. Tearney, and J. F. de Boer, "Ultrahigh-resolution high-speed retinal imaging using spectral-domain optical coherence tomography," *Opt. Exp.* **12**, 2435–2447 (2004), URL <http://www.opticsinfobase.org/abstract.cfm?URI=oe-12-11-2435>.
59. B. Sander, M. Larsen, L. Thrane, J. L. Hougaard, and T. M. Jorgensen, "Enhanced optical coherence tomography imaging by multiple scan averaging," *Br. J. Ophthalmol.* **89**, 207–212 (2005).
60. A. Sakamoto, "Improvement of image quality by composition method," Tech. rep., Kyoto University Hospital (2006).
61. P. Maragos and R. W. Schafer, "Morphological filters—Part I: Their set-theoretic analysis and relations to linear shift-invariant filters," *IEEE Trans. Acoust. Speech Signal Process.* **ASSP-35**, 1153–1169 (1987).
62. S. Jiao, R. Knighton, X. Huang, G. Gregori, and C. Puliafito, "Simultaneous acquisition of sectional and fundus ophthalmic images with spectral-domain optical coherence tomography," *Opt. Exp.* **13**, 444–452 (2005), URL <http://www.opticsinfobase.org/abstract.cfm?URI=oe-13-2-444>.
63. M. Yamanari, S. Makita, V. D. Madjarova, T. Yatagai, and Y. Yasuno, "Fiber-Based Polarization-Sensitive Fourier Domain Optical Coherence Tomography using B-Scan-Oriented Polarization Modulation Method," *Opt. Exp.* **14**, 6502–6515 (2006), URL <http://www.opticsinfobase.org/abstract.cfm?URI=oe-14-14-6502>.
64. H. H. Arsenault and G. April, "Properties of speckle integrated with a finite aperture and logarithmically transformed," *J. Opt. Soc. Am.* **66**, 1160–1163 (1976).
65. M. Hammer, A. Roggan, D. Schweitzer, and G. Müller, "Optical properties of ocular fundus tissues—an in vitro study using the double-integrating-sphere technique and inverse Monte Carlo simulation," *Phys. Med. Biol.* **40**, 963–978 (1995).
66. A. Roggan, M. Friebe, K. Dörschel, A. Hahn, and G. Müller, "Optical Properties of Circulating Human Blood in the Wavelength Range 400–2500 nm," *J. Biomed. Opt.* **4**, 36–46 (1999).
67. A. Bill, "Blood circulation and fluid dynamics in the eye," *Physiol. Rev.* **55**, 383–417 (1975).
68. M. Mujat, R. Chan, B. Cense, B. Park, C. Joo, T. Akkin, T. Chen, and J. de Boer, "Retinal nerve fiber layer thickness map determined from optical coherence tomography images," *Opt. Exp.* **13**, 9480–9491 (2005), URL <http://www.opticsinfobase.org/abstract.cfm?URI=oe-13-23-9480>.

1. Introduction

Fourier-domain optical coherence tomography (FD-OCT) [1, 2] is a high-speed and highly sensitive alternative to time-domain OCT (TD-OCT) [3]. OCT has been employed in several biological and medical studies and practices, e.g., dermatology [4, 5], cardiology [6], urology [7], and dentistry [8, 9]. Among all these applications, OCT has been employed most successfully in the field of ophthalmology [10]. During the last decade, TD-OCT using a probe beam in the wavelength band of 830 nm has become a standard assessment tool for retinal diseases (Stratus OCT, Carl Zeiss Meditec Inc., Dublin, CA; OCT/SLO, Ophthalmic Technologies Inc., Canada). Recently, spectral-domain OCT (SD-OCT), which is one of the variations of FD-OCT having the same probe band of 830 nm, has been employed in clinical studies and diagnoses [11–16]. Swept-source OCT (SS-OCT), also referred to as optical frequency-domain imaging (OFDI), is another variation of FD-OCT. SS-OCT with a wavelength band of 830 nm has been demonstrated [17], and it has been recently applied to *in vivo* retinal investigations [18, 19].

Because OCT reveals the morphological structures of subjects, it is particularly suitable for ocular diseases associated with structural changes, e.g., macular hole [14–16], age-related macular degeneration (AMD) [14, 15], diabetic retinopathy (DR) [15] and glaucoma [20, 21]. It is also known that some ocular diseases are related to circulation or vasculature abnormalities. For example, AMD is characterized as choroidal neovascularization (CNV) at its onset, and DR and glaucoma are suspected to be associated with abnormal circulation. Hence, it is important

to visualize the structure and function of retinal and choroidal vasculatures.

For this purpose, angiography using a contrast dye has been widely employed in clinics [22]. Fluorescein angiography (FA) uses fluorescein as the contrast agent, and blue light is used to excite the contrast agent that emits yellow-green light. Indocyanine green angiography (ICGA) uses near-infrared light both for excitation and detection. Because of the difference in the wavelengths, FA mainly reveals the functions and structures of the retinal vasculature, while ICGA is used to investigate those of the choroidal vasculature.

These angiographic techniques yield not only the structural information of the vasculature but also the functional information of the eye related to ocular metabolism. However, both FA and ICGA are invasive techniques. Moderate but frequent and rare but serious side effects have been reported [23, 24].

In certain applications, Doppler OCT [12, 25–28] can be used as an alternative to FA/ICGA, and a Doppler optical coherence angiography (D-OCA) scheme provides the means to use Doppler OCT as an alternative to FA/ICGA [29]. However, collecting faint Doppler signals from the choroid is still a challenging task, although it is possible [28, 29]. As mentioned earlier, some ocular diseases including AMD and polypoidal choroidal vasculopathy (PCV) are related to abnormalities in the choroidal vasculature. This indicates that OCT and its related angiographic techniques with higher penetration capabilities might be useful in the detection of these diseases.

It is known that OCT using a probing wavelength of $1.3\ \mu\text{m}$ provides higher penetration for a tissue than that with the $830\ \text{nm}$ OCT owing to its longer wavelength. OCT employing this wavelength band is widely used in ophthalmology for the investigation of the anterior eye [30]. Anterior-eye TD-OCT is now commercially available (Visante OCT, Carl Zeiss Meditec Inc), anterior-eye SS-OCT has also been demonstrated in laboratories [31–33]. Despite the success of anterior-eye OCT, it is known that this wavelength is not applicable for retinal OCT. Because the water absorption of $1.3\text{-}\mu\text{m}$ light is 38 times greater than that of 830-nm light [34], this long-wavelength light cannot travel in the vitreous body and therefore it is not applicable for retinal OCT.

The $1\text{-}\mu\text{m}$ band is an interesting alternative to the 830-nm and $1.3\text{-}\mu\text{m}$ bands for high-penetration retinal and choroidal OCT. Water absorption has a local minimum at $1.06\ \mu\text{m}$ [34]. This absorption window allows this long-wavelength light to access the retina. Furthermore, this wavelength reduces the effect of dispersion because zero dispersion for water exists at around $1\ \mu\text{m}$ [34, 35]. Retinal and choroidal investigations using TD-OCT in this wavelength band have been reported [36].

Because of the advantages with regard to sensitivity [37–40] and measurement speed [41–43], it is reasonable to utilize this wavelength band in an FD-OCT scheme. As mentioned earlier, two types of FD-OCT exist, namely, SD-OCT and SS-OCT. The present 830-nm retinal FD-OCT employs an SD-OCT scheme [2, 42]. However, it is not realistic to assemble an SD-OCT with a $1\text{-}\mu\text{m}$ probe. This is because SD-OCT requires a high-speed spectrometer equipped with a high-speed line detector. The options available for the high-speed line detector for a $1\text{-}\mu\text{m}$ band are limited and its detection speed is slow, while fast and inexpensive line CCD cameras operating in the $830\ \text{nm}$ band are available. Hence, the SS-OCT scheme is more suitable for $1\text{-}\mu\text{m}$ FD-OCT. It is known that SS-OCT possesses a higher tolerability to sample motion [44], and it potentially possesses a higher speed than SD-OCT [45–47]. Recent *in vitro* porcine retinal imaging [48] and *in vivo* retinal and choroidal [49] imaging using $1\text{-}\mu\text{m}$ SS-OCT have proven the importance of this SS-OCT.

In this paper, we demonstrate a new OCA technique based on $1\text{-}\mu\text{m}$ SS-OCT to visualize the choroidal vasculature. The D-OCA technique demonstrated earlier [29] uses the phase of the OCT signal and requires a high phase stability. In general, the signal-to-noise ratio (SNR)

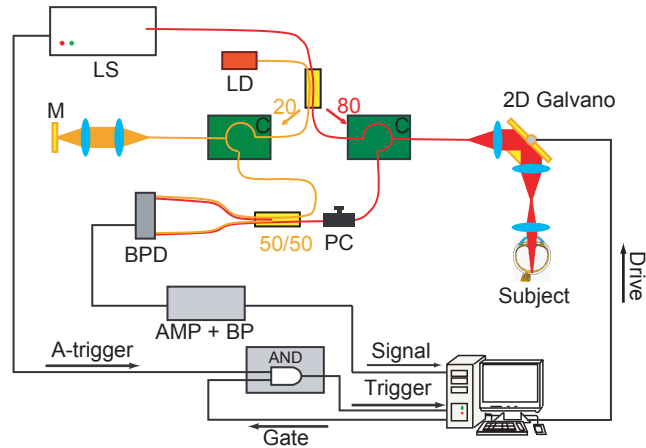


Fig. 1. Schematic diagram of 1- μm SS-OCT. LS denotes the light source; LD, laser diode for an aiming beam; C, circulator; M, mirror; PC, polarization controller; BPD, balanced photodetector; AMP, RF amplifier; and BP, RF band-pass filter.

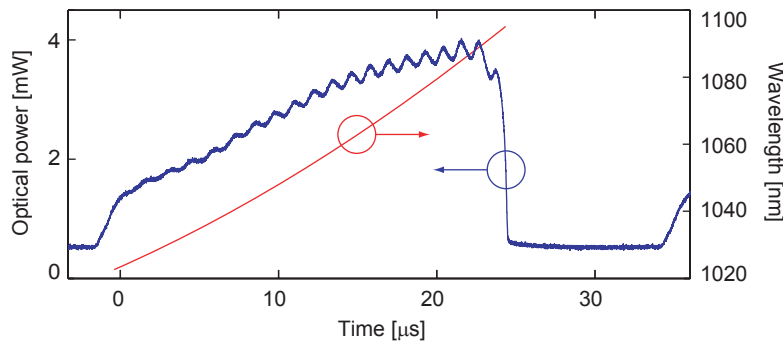


Fig. 2. Time dependence of the output power and wavelength of the light source.

in the choroid is lower than that in the retina, and this low SNR disturbs the phase of the OCT. Furthermore, obtaining a high phase stability with high-speed SS-OCT [50,51] is a relatively elaborate process. Hence, in this paper, we demonstrate another OCA technique, which is termed scattering OCA (S-OCA); this technique is independent of the phase of the OCT. S-OCA is a software-based segmentation algorithm and employs only the intensity, hence, it does not require phase stability. S-OCA using 1- μm SS-OCT is used to visualize the *in vivo* three-dimensional (3D) network structure of human choroidal vessels. Imaging of the *in vivo* human sclera was also performed owing to the high penetration of 1- μm SS-OCT. While OCT signal beneath the normal choroid has recently been shown by using 1- μm SS-OCT [49], our system provides a deep penetration within the sclera such that the fringe artifacts originating from the strong birefringence of the sclera become visible.

2. 1- μm band swept source optical coherence tomography

2.1. System hardware

The scheme of our SS-OCT (Fig. 1) is similar to that of the previously described 1.3 μm band SS-OCT which uses Mach-Zehnder interferometer [31] except for its light source. A high-

speed wavelength-scanning light source (HSL-1000 ver. 1.0, Santec Corporation, Aichi, Japan) is employed, which uses a polygon-mirror-based high-speed wavelength tuner operating at 28 kHz and monodirectionally scans the lasing wavelength from a shorter to a longer wavelength with a maximum output power of 4 mW, as shown in Fig. 2. This scanning frequency directly determines the measurement speed of our SS-OCT as 28,000 A-scans/s. The center wavelength is 1060 nm, the scanning range is 72 nm, and the scanning speed is 2.95 nm/ μ s.

80% of the light is introduced into the probe arm of the interferometer, which consists of a semi-bulk circulator (AGILTRON Inc., MA), a fiber-attached collimator lens with ($f = 15.3$ mm, F260FC-C, Thorlabs Inc. NJ), a two-axis galvano scanner (Cambridge Technology Inc., MA), an achromatic doublet ($f = 50$ mm, AC254-050-C, Thorlabs), and a double aspheric slit-lamp lens (78D, Volk Optical Inc., OH). The probe power incident on the eye is 1.1 mW, which conforms to the ANSI eye-safety criterion [53]. For the purpose of aiming, a very weak visible diode laser with a wavelength of 635 nm is introduced into the probe arm from a residual port of the first coupler that splits the probe and reference beams.

The probe and reference beams are combined by a 50/50 coupler, and an interference signal is detected by using a balanced photodetector (Model 1817-FC, Newfocus, Bookham Inc., CA). The output voltage from the photodetector unit is amplified and then transferred into a radio-frequency (RF) bandpass filter with a pass band from 2.5 MHz to 38 MHz.

A portion of the light is monitored in the light source unit via an optical narrowband filter, and the output from the monitor is converted into a TTL signal (A-trigger). The A-trigger is first gated by a gate signal that is synchronously generated with the driving signals of the two-axis galvano scanner by a function generator board (NI-6713, National Instruments, TX). Each gated A-trigger initiates the AD sampling of a single spectral interference signal corresponding to a single A-line. The spectral signal is digitized by a 14-bit AD conversion board (Compuscope 14200, Gage Applied Technologies Inc., IL) with a sampling frequency of 100 mega-samples/s and 2048 sampling points. This sampling configuration determines the maximum depth measurement range as 9.4 mm; however, it is further limited by the depth-dependent signal decay, as described in section 2.4.

The data set for the entire 3D OCT volume is first stored in the onboard memory of the AD board and is then transferred to the main memory of a computer after the acquisition is completed. Because of this data transfer scheme, the duty factor of the 3D measurement is not limited by the data transfer speed, but it is limited by the scanning waveform of the galvano scanner, i.e., sawtooth scanning. This saw tooth scanning has a duty cycle of 95%, which reduces down the overall measurement speed of the 3D measurement to 26,600 A-scans/s.

The digitized spectrum is first reshaped by a spectral shaping filter (described in section 2.2), rescaled into a wavenumber (k -) domain [42, 54], multiplied by a wavelength-dependent counter-dispersive phase to cancel the residual dispersion (described in section 2.3), and numerically Fourier transformed by using the fast Fourier transform (FFT) algorithm to yield an OCT image.

2.2. Automated spectral reshaping

Because of the imperfections in the antireflection coating of the semiconductor optical amplifier (SOA) used in the light source, some small ripples are evident in the light source spectrum, as shown in Fig. 2. These ripples as well as the wavelength dependence and several types of dispersions in the optical fiber components modulate the fringe contrast of the spectral interference signal. Because the axial point spread function (PSF) of OCT is a Fourier transform of the fringe contrast, this modulation may result in side peaks and broadened side lobes in the PSF. To eliminate these modulations, we applied a dynamic spectral shaping filter similar to the method presented by Tripathi *et al.* [55]; however, we used a fast algorithm for the detection of

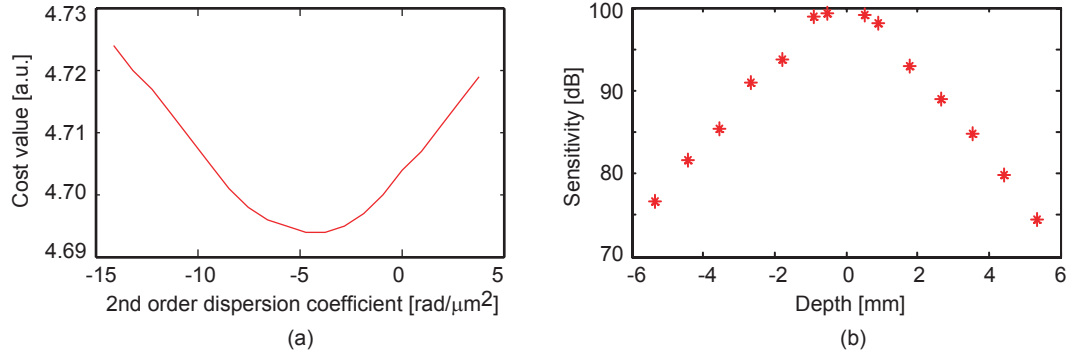


Fig. 3. (a) An example of information entropy, i.e., a cost function, of an OCT image, with respect to the change in the coefficients of the second-order phase for dispersion compensation. (b) Depth dependent sensitivity decay of SS-OCT. The horizontal axis is the relative depth from the zero delay point, and the vertical axis is the system sensitivity.

fringe contrast using a Wiener filter.

To design the Wiener filter, it is essential to determine the envelope of the wavelength-dependent fringe contrast. As the first step in the design of a spectral shaping filter, we employed a fringe-analysis-based method to extract the wavelength-dependent fringe contrast from the OCT spectral signals.

The spectral interference signal can be rewritten as the multiplication of the contrast envelope and a fringe: $S_j(k) = S_e(k) \cos \phi_j(k)$, where $\phi_j(k)$ is the phase of the j -th fringe. The ensemble average of $S_j(k)^2$ in j is then expressed as

$$\langle S_j(k)^2 \rangle_j = S_e(k)^2 \langle \cos^2 \phi_j(k) \rangle_j. \quad (1)$$

If $\phi_j(k)$ is, as is reasonably assumed in the OCT measurement, random in j , the ensemble average of the squared cosine term is reduced to a constant value— $1/2$. From this equation, we obtain a simplified equation of the contrast envelope:

$$S_e(k) = \sqrt{\frac{2}{N} \sum_j S_j(k)^2}. \quad (2)$$

This equation is then substituted into the following equation of a Wiener filter, yielding a spectral reshaping filter.

$$W(k) = \frac{S_e(k)}{S_e(k)^2 + n_c} \text{Gauss}(k) \quad (3)$$

where n_c is a constant depending on the SNR of the detection system and $\text{Gauss}(k)$ is a Gaussian window used to reshape the spectrum to a Gaussian profile.

After this spectral reshaping, the mean depth resolution within 2 mm is measured to be $14.4 \mu\text{m}$, which corresponds to $10.4 \mu\text{m}$ in tissue (index = 1.38). The departure from the depth resolution calculated from the center wavelength and the FWHM value of the light source is satisfactorily explained by the relatively narrow FWHM value of the Gaussian window as compared to the wavelength scanning range of the light source.

2.3. Automatic dispersion compensation

The system dispersion, residual dispersion of the eye, and rescaling error are numerically canceled by using a counter-dispersive phase, i.e., the spectrum is multiplied by the counter-

dispersive phase before performing FFT [56–58]. In contrast to the previously demonstrated methods, the information entropy of the resulting linear-scale OCT image

$$\varepsilon = - \sum_{x,z} P(x,z) \log P(x,z) \quad (4)$$

is employed as the cost function for the optimization of the counter-dispersive phase, where $P(x,z) \equiv I(x,z) / \sum_{x,z} I(x,z)$ is the normalized OCT B-scan image ($I(x,z)$) and x and z represent the positions along the fast scanning direction and depth, respectively. This cost function has a smooth profile, as shown in Fig. 3(a), and it enables the reduction of the number of iterations for the optimization, and reduces the calculation time. This optimum counter-dispersive phase is calculated only once for an OCT volume with the first B-scan image and is applied to all the images in the volume.

Several optimization methods for dispersion compensation have been proposed. However, our cost function has a smoother profile than the previously demonstrated cost function, which uses the number of high-intensity pixels in the OCT image [57]. This smooth profile may reduce the required number of iterations and reduce the overall optimization time.

2.4. System sensitivity

The system sensitivity at a probe power of 1.2 mW was measured to be 99.3 dB by a -63 dB partially attenuating mirror, while the shot-noise-limited sensitivity was 112.6 dB. The recoupling loss at the probe fiber tip, imperfections in the semi-bulk circulator, residual rescaling error, unoptimized reference power, and the relative intensity noise (RIN) of the light source may account for this departure.

As shown in Fig. 3(b), the system sensitivity decreases as the distance of the depth position from the zero delay point increases with a signal decay slope of -5.2 dB/mm. According to this slope, the instantaneous line width of the light source is estimated to be 0.43 nm. On the basis of the maximum sensitivity, the average collection efficiency of the probe scattered by retina, which is assumed to be -60 to -80 dB, and this decay slope, the sensitivity limited depth measurement range is approximately estimated to be 7.6 mm to 3.7 mm. Although this depth range is smaller than the sampling-configuration-limited depth range of 9.4 mm mentioned in section 2.1, it is still sufficiently wide for retinal and choroidal investigations.

2.5. Three-dimensional despeckle filtering

In general, the number of A-lines per B-frame for 3D measurements is smaller than that required for 2D measurements, because the total acquisition time should be sufficiently small to avoid involuntary eye motion. Because of the low density of the A-lines and the additional speckles in the OCT image, it is sometimes difficult to recognize the faint morphological features of the eye. Here, we enhance the readability of the OCT image by using despeckle image filtering.

It is known that averaging several images captured from nearly identical positions reduces the speckles in a B-scan image [59]. Further, it was pointed out that averaging several adjacent frames in the 3D OCT volume reduces the speckles and enhances the clinical readability of the OCT image [60]. We introduced a maximum-intensity-projection-based (MIP-based) despeckle filter for a further improvement in the clinical readability of the 2D OCT images in a 3D OCT volume. In this filtering operation, three adjacent frames in an OCT volume are used to yield a single speckle-reduced OCT frame. These three frames are compared with respect to their intensities, and the maximum intensities of the three frames at each individual location on the image are selected to yield a resulting OCT image. This operation is also considered to be a one-dimensional morphological dilation filter [61] operating along the visual axis of the observer

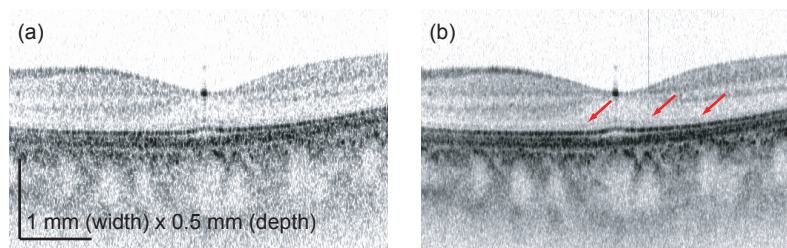


Fig. 4. (a) *In vivo* human macula measured by SS-OCT and (b) the same image obtained using an MIP based despeckle filter.

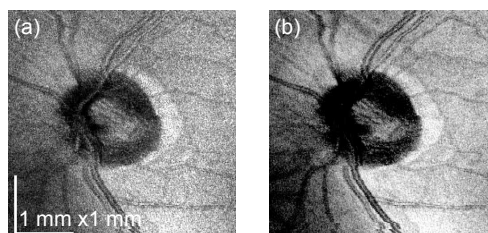


Fig. 5. (a) Fundus preview image of the optic nerve head created by squared spectral integration. (b) Standard OCT fundus image created from the same measurement.

viewing the OCT image. This despeckle filtering is then applied to all the frames in the OCT volume in a rolling manner.

Figure 4(a) shows a raw OCT image of the *in vivo* human macula captured using SS-OCT, which consists of 512 A-lines. This image is extracted from the 3D OCT volume containing 255 frames. Despite the deep penetration, the speckle grains distract the observers, thereby making it difficult to understand the clinical features. The despeckle filter enhances the readability of the image as shown in Fig. 4(b). In this image, the major layers in the retina are visible, and it is noteworthy that the external limiting membrane (ELM) is also visible in spite of the relatively lower depth resolution and the low density of the image (indicated by the arrows).

The transversal resolution may get sacrificed in this despeckle filtering technique. The typical frame spacing in our 3D measurement protocol is $20\ \mu\text{m}$, hence, despeckle filtering reduces the transversal resolution to $80\ \mu\text{m}$, which is twice the separation between the first and third frames. Because the optical transversal resolution of our SS-OCT is $27\ \mu\text{m}$, there is more than twofold reduction of the resolution. Although they were rare, some artifacts originating from this filtering were observed; e.g., the decrease in the contrast of the small focal lesions, the thickening of the thin retinal layer, and ghost images around the rapidly morphologically changing lesions. Hence, it is recommended that the operators/clinicians frequently verify the original image. In spite of the drawbacks, despeckle filtering provides a superior contrast for the clinical features in the OCT images.

2.6. Fundus preview for three-dimensional measurement

In the 3D measurement mode, a preview image of the fundus (fundus preview) is created immediately after acquisition as follows. The central 256 points are extracted from a single spectral interference signal, and the signal power is obtained by squaring followed by its summation. This operation provides only the power of the interference signal, because the non-interference offset of the spectrum gets rejected by a balance detection scheme and an RF high-pass filter. This operation is applied to all the spectral signals in the OCT volume, yielding the fundus

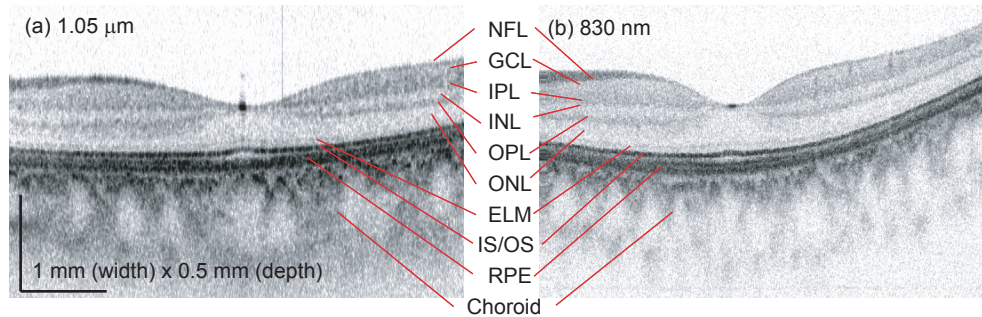


Fig. 6. OCT B-scan of *in vivo* human macula captured using (a) 1- μ m OCT and (b) 830-nm SD-OCT.

preview image as shown in Fig. 5(a). This fundus preview is an analog-operation analog of its digital counterpart demonstrated by Jiao *et al.* [62].

The comparison with a corresponding depth-integrated OCT fundus image [11,62], as shown in Fig. 5(b), confirms that the fundus preview is comparable to the OCT fundus image.

3. High-penetration imaging of *in vivo* human eye

3.1. *In vivo* imaging of human retina and choroid

Figure 6 shows a comparison of the B-scan images of the *in vivo* human macula captured using 1- μ m SS-OCT and 830-nm SD-OCT [29, 63] where the both images are displayed with the identical image range; from -10 dB to +35 dB from the noise floor. The subject is a healthy 25-year-old Asian male (subject-1). Although all the presented examinations were performed in a dim laboratory, the subjects' eyes were not dilated. In this figure, each individual layer including the nerve fiber layer (NFL), ganglion cell layer (GCL), inner plexiform layer (IPL), inner nuclear layer (INL), outer plexiform layer (OPL), outer nuclear layer (ONL), the junction between the inner and outer segments of the photoreceptor (IS/OS), RPE complex, and choroid are visible. In this paper, we adapt one of the conventional notations of the layer-complex around RPE which includes ELM, IS/OS, RPE, and choriocapillaris. However, it is noteworthy that several arguments are recently emerging for the correspondence of these layers and their appearance in OCT images [14, 52, 56–58]. Although this 830-nm SD-OCT has a superior sensitivity, the better penetration and higher contrast of the choroid obtained from 1- μ m SS-OCT are evident from these images. A strong OCT signal is visible even beneath the choroidal vessels in the 1- μ m image because of the wavelength dependent scattering property of the choroid.

Figure 7 shows the measurement results for the optic nerve head of a healthy human volunteer, a 26-year-old Asian male (subject-2). Figures 7(a) and (b) show the B-scan images along the fast scanning direction containing 512 A-lines. The positions of these images are indicated by the red lines in the OCT fundus image (Fig. 7(g)). Figures 7(c)–(f) are the corresponding OCT images captured using 830-nm polarization-sensitive SD-OCT (PS-SD-OCT) with a system sensitivity of 101 dB [63]; these are given for the purpose of comparison. Figures 7(c) and (d) are the Mueller matrix (0, 0)-element images (M_{00} images) which are polarization insensitive OCT, and Figs. 7(e) and (f) are the phase-retardation images, where the image hue and brightness correspond to the retardation and OCT intensity, respectively. Because the M_{00} image is an intensity-summation of all the elements of the corresponding Jones matrix, its noise statistics differ from those of a conventional OCT intensity image [64]. The standard deviation of the noise floor of the M_{00} image is smaller than that of the conventional OCT image, and it

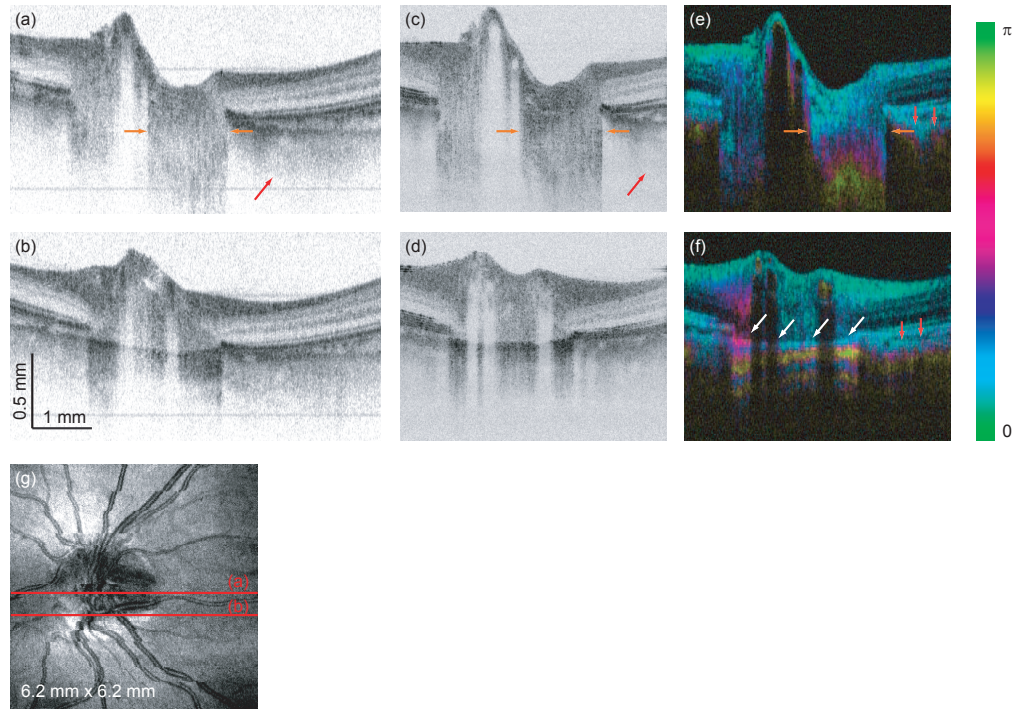


Fig. 7. *In vivo* human optic nerve head measured by using SS-OCT and PS-SD-OCT. (a) and (b) are the horizontal OCT B-mode images captured using 1- μ m SS-OCT. Click on the figures for a 2.4 MB movie (10.7 MB version is also available). (c) and (d) are the corresponding OCT images captured using 830-nm PS-SD-OCT, and (e) and (f) are the corresponding phase retardation images (1.9 MB movie). (g) is an OCT fundus.

appears as a relatively bright background because the lowest range is set to lower than the mean noise level. Despite this appearance of the noise floor, the PS-SD-OCT has superior sensitivity and all images presented are displayed with an identical image range of 45 dB. The stronger signal in the deeper region of the 1- μ m image is visible. The difference in the signal strength is visible particularly beneath the RPE, as indicated by the red arrows in Figs. 7(a) and (b), because of the wavelength-dependent absorption property of the RPE (see section 3.3). It can also be seen that the signal degradation beneath the blood vessels due to fringe washout [44] is less in the SS-OCT images than the SD-OCT images. The locations of the lamina cribrosa (orange arrows) and the chorio-scleral junction (red arrows) can be identified in the phase-retardation images because the lamina cribrosa and sclera possess strong birefringence because of collagen. The identical positions are indicated by the orange arrows in the corresponding 1- μ m image. According to the location, the different contrasts of the lamina cribrosa and the tissue superior to that can be seen. According to Fig. 7(f), it is found that the sclera in this part is exposed because of the myopic conus, as indicated by the white arrows.

3.2. *In vivo* imaging of human sclera

Because of the high penetration of 1- μ m light, the *in vivo* imaging of the human sclera is possible by using SS-OCT. Figure 8(b) shows the OCT B-scans of a 31-year-old Asian male (subject-3). Fringe artifacts are visible in the areas indicated by the yellow boxes. It is known that the sclera consists of collagen and possesses a strong birefringence [52]. This strong bire-

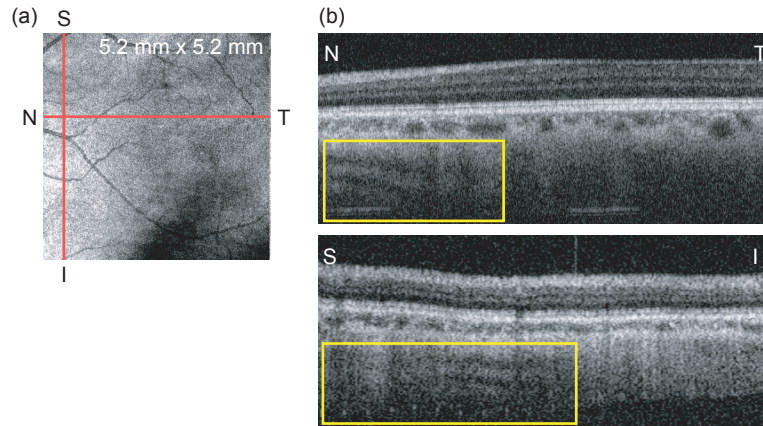


Fig. 8. Visualization of the sclera of *in vivo* human macula. (b) OCT B-scan images show the penetration to the sclera. (a) Positions of the B-scan images are indicated by red lines in the OCT fundus.

fringe alters the polarization state of the probe beam as the probe propagates into the sclera and creates the fringe artifacts. Hence, these fringe artifacts clearly indicate that this SS-OCT penetrates into the sclera. We examined three eyes of three normal subjects and obtained the fringe artifacts from two out of these three eyes. The OCT signal beneath the choroid has been observed by using 1- μm SS-OCT in a demonstration by Lee *et al.* [49]. This fringe artifact of the sclera further confirms that the penetration of 1- μm SS-OCT reaches the sclera.

3.3. Discussions

To understand the high penetration of 1- μm OCT, we discuss the wavelength dependency of the scattering and absorption properties of the posterior eye. Although a similar discussion has been previously given by Unterhuber *et al.* [36], we consider the effects of sclera and blood in the choroid in this discussion.

It is known that the scattering coefficients of the neural retina and the RPE are nearly identical at 830 nm and 1.05 μm [65]. On the other hand, the scattering coefficients of the choroid and sclera at 1.05 μm are 7 mm^{-1} and 15 mm^{-1} lower than those at 830 nm, respectively [65]. In contrast to scattering, the absorptions of RPE and choroid have very strong and moderate wavelength dependencies, respectively, whereas those of the neural retina and the sclera are nearly identical in these two wavelength bands [65]. On the basis of these properties, we conclude that the high penetration of 1- μm OCT can be attributed to the lower scattering of the choroid and sclera and the lower absorptions of the RPE and choroid at 1.05 μm than those at 830 nm. It is also noteworthy that according to the identical optical properties of the neural retina in these two wavelength bands, the low-scattering property at longer wavelengths does not degrade the OCT image of the retina.

Another characteristic property of the 1- μm OCT image is the strong signal from the choroids located beneath a large choroidal vessel; the wavelength dependency of the optical properties of blood may account for this image property. It is known that the absorption coefficients of blood with 100% oxygen saturation are nearly identical at 830 nm and 1.05 μm [66]. On the other hand, the absorption of blood with 0% oxygen saturation has a sharp local minimum at 1.05 μm , which is one-fifth that at 830 nm [66]. Despite this strong wavelength dependence of deoxygenated blood, it may not influence the wavelength property of the choroid, because the oxygen content of the choroid is exceptionally high [67]. In contrast to the absorp-

tion property, the scattering coefficient of blood for 1.05- μm light is approximately 30% lower than that for 830 nm [67]. This wavelength dependence of the scattering of the blood may contribute to the contrast of the choroids located beneath the vessels. Although the immunity of SS-OCT to fringe washout is also suspected to contribute toward such high contrasts, further investigations are mandatory for a discussion.

4. Scattering optical coherence angiography

4.1. Introduction

For the clinical examination of eye diseases associated with the abnormalities in the choroidal vasculature, it might be useful to visualize the choroidal vessels with high contrast. Lee *et al.* demonstrated a high-contrast choroidal vessel map by using 1- μm SS-OCT and averaging in a particular depth range [49]. For a further 3D visualization, we present a software-based 3D segmentation method for choroidal vessels.

As observed in Figs. 6–8, the choroidal vessels are visualized as low-scattering regions in the OCT images. The basic concept of our S-OCA technique is to use an intensity-threshold-based binarization (ITB) technique to segment these regions. Although the concept is very simple, there are several difficulties in the application of the ITB technique to OCT images mainly because of the depth-dependent signal decay due to scattering in the sample. To avoid this intrinsic problem, we applied a method similar to that demonstrated by Hori *et al.* [5], however, it has been specially redesigned for the purpose of OCA.

In order to avoid the problem of signal decay, the algorithm processes en face OCT images and not the OCT B-scans. Further, the en face images are extracted from a constant distance from the RPE and not from a constant distance from the zero delay point. The signal decay is nearly even in this en face image, hence, the ITB technique can be applied. The following section describes the details of the algorithm.

4.2. Methods

4.2.1. Segmentation of OCT volume

The first step in the S-OCA algorithm is the segmentation of the OCT volume into four regions, namely, (1) the vitreous body, (2) the retina, (3) the choroid and the sclera, and (4) the deeper area without the OCT signal.

To split the vitreous body and the retina, a method similar to that presented by Mujat *et al.* [68] was employed. The details have been described in Ref. [68]; however, we briefly summarize this method. The OCT image is first blurred by a Gaussian kernel, and the magnitude of the gradient of the blurred image is used as an indicator of the edge. The gradient image is then binarized by using a threshold, and the first unity from the top of the image is regarded as the boundary between the vitreous body and the retina, namely, the internal limiting membrane. The deformable spline (snake) algorithm employed by Mujat *et al.* is not used in our algorithm to reduce the calculation time. The vitreous region could be optionally set to zero for a better volumetric visualization.

The maximum gradient of the abovementioned blurred image is then regarded as the position of the complex of RPE and IS/OS [29]. The shadow of the retinal vessels might lead to an error in the algorithm because of the low signal intensity and the resulting low SNR in this region. To avoid this error, the shadows of the vessels are detected [68] and the RPE in the corresponding region is interpolated from the positions of the RPE in the adjacent regions. In the case of the optic nerve head, the position of the RPE is also virtually interpolated inside the scleral ring to simplify the subsequent signal processing, although it is clear that no RPE exists in this region.

A region deeper than the OCT penetration is detected in the following manner. The OCT

image is first blurred by a Gaussian kernel, and the noise level of the image is determined from the vitreous region. A threshold value determined from the noise level is then applied to find the region deeper than the OCT penetration, and this region is set to zero.

4.2.2. Segmentation of choroidal vessels

The segmented choroid including the sclera is then flattened to the RPE. According to this flattening, the OCT signal decay at a single depth becomes nearly constant and the ITB technique can be readily applied.

Our segmentation algorithm for choroidal vessels operates on each depth slice of the OCT volume at constant depths from the RPE. The mean pixel intensity $\mu_{z'}$ and the standard deviation of the pixel intensity $\sigma_{z'}$ of a single depth slice represented in a logarithmic scale are first derived. Based on the fact that the choroidal vessels are visualized as low-scattering regions in the OCT image, the pixels that have a pixel intensity $I_{z'}(x,y)$ of

$$I_n < I_{z'}(x,y) < \mu_{z'} - \frac{1}{2}\sigma_{z'} \quad (5)$$

are selected as the regions of the choroidal vessels, where I_n denotes the noise level of the image, subscript z' indicates the depth from the RPE, and x and y represent the positions along the fast and slow transversal scanning positions, respectively. This ITB operation is then iteratively applied at all the depths from the RPE, thereby yielding a 3D binary mask to segment the choroidal vessels.

For the high-contrast visualization of the 3D structure of the choroidal vessels, the intensity-inverted OCT volume is multiplied by this 3D binary mask; finally, this operation yields a high-contrast OCT volume of the choroidal vessels.

4.3. Results

Figure 9(a) shows the 3D reconstruction of the choroidal vessels of the macula of subject-3 overlapped with the OCT intensity volume, where an inverted-gray color map represents the OCT intensity and an orange-red color map represents the segmented choroidal vasculature (2.3 MB and 4.4 MB movies are available). Figure 9(b) shows the en face slices of the 3D reconstruction at several different depths, where a semitransparent inverted-gray color map is applied to the OCT intensity. These figures reveal the correspondence between the vasculature and the morphological structure of the retina. The movie in Fig. 9(b) shows the depth-dependent structure of the choroidal vasculature. Figure 9(c) shows a stereoview of the segmented choroidal vasculature, which might assist in the intuitive and comprehensive understanding of the subject. The depth-integrated segmented vasculature (Fig. 9(d)) provides information somehow similar to that provided by ICGA, although several differences exist (see section 4.4.1).

Figure 10(a) (3D view) shows a 3D reconstruction of the optic nerve head of subject-3, where the segmented choroidal vasculature and intensity OCT are displayed with an orange-red and inverted-gray color maps, respectively. The following sequence of images shows the en face sections of the 3D volume at several depths, where the sectioning planes are slightly slanted from the en face plane of the OCT system (2.3 MB and 5.1 MB movies are available). In this image, vessels 1–5 indicate the choroidal vessels segmented using S-OCA. These vessels are also visible in the 3D S-OCA image (Fig. 10(b)). Some small vessels (vessel-1) are also indicated by the orange color (Figure 10(a)), although they are hardly seen in 3D S-OCA. Signals (i) and (ii) are the artifacts occurring due to the shadow of a retinal vessel and an optic cup, respectively. The elimination of these artifacts in the optic nerve head is the remaining problem of S-OCA. The ICGA-style projection of S-OCA is shown in Fig. 10(d).

These visualizations of the choroidal vasculature might be useful for the detection of choroidal diseases related to vascularization, e.g., PCV and CNV, and following up of treated

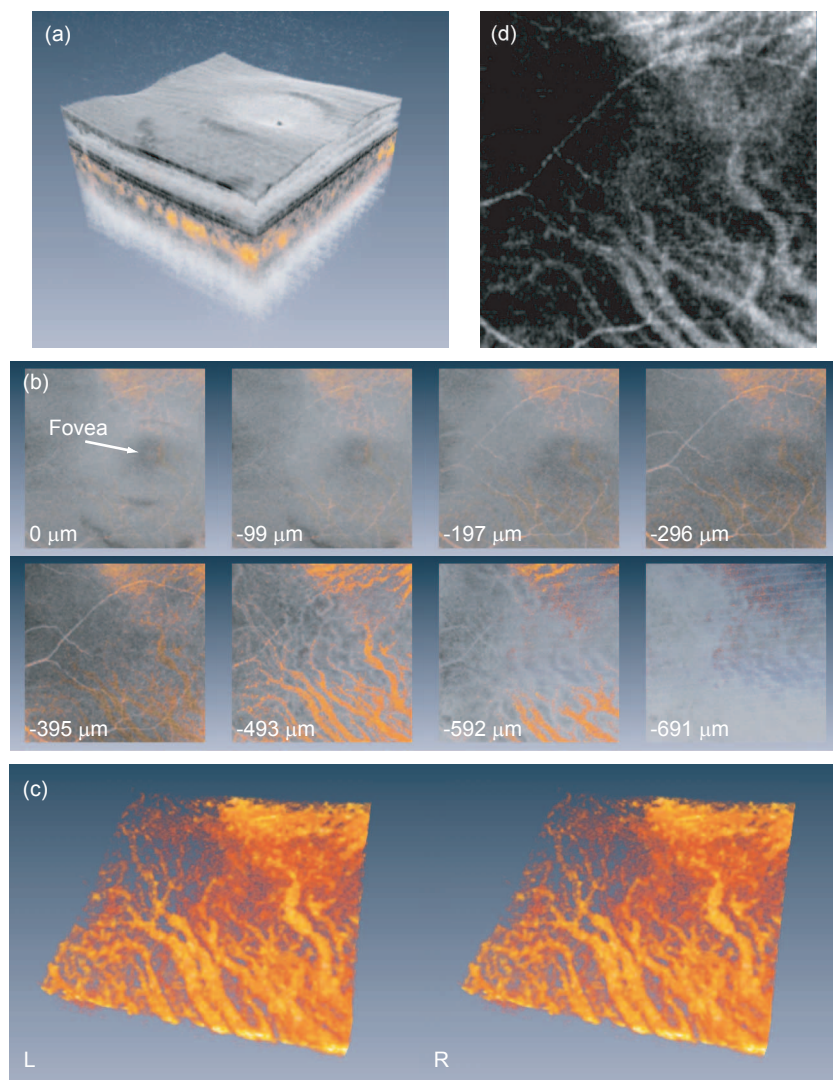


Fig. 9. (a) 3D volume-rendered OCT images of *in vivo* human macula in which the OCT intensity signal is displayed in an inverted-gray color map and the choroidal vessels are displayed with an orange-red color map. Click on the figure for movies (short version is 2.3 MB and long version is 4.4 MB). (b) En face slices of the volumetric rendering at several different depths, where a semitransparent color map is applied to the OCT intensity volume. (c) A stereoview of the choroidal vessels of the macula.

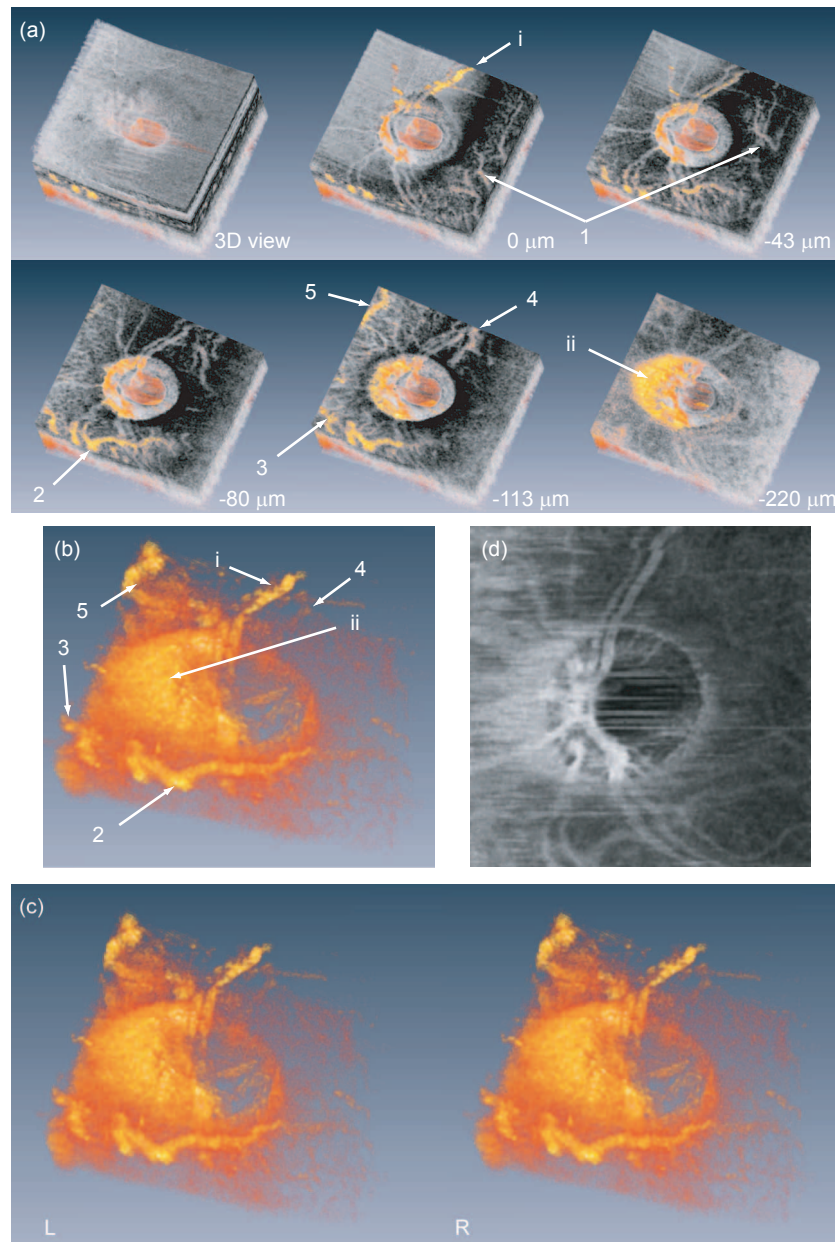


Fig. 10. (a) 3D reconstruction of the choroidal vessels of a human optic nerve head (orange-red color map) overlaid by the intensity OCT (inverted gray color map). The volume is sectioned along the depth, where the sectioning plane is slightly slanted from the en face plane. Click on the figure for a movie (2.3 MB or 5.1 MB versions). (b) 3D rendering of the choroidal vasculature and (c) its stereoview. (d) En face average projection of the choroidal vasculature.

choroidal vasculatures, e.g., observing the occlusion of choroidal vessels after laser photocoagulation.

4.4. Discussions

4.4.1. S-OCA and other angiography methods

	S-OCA	D-OCA / D-OCT	CIP	FA	ICGA
Invasiveness	none	none	none	moderate	moderate
Contrast source	scattering	blood flow	scattering	contrast dye	contrast dye
Visualized target	3D vessel structure	3D flow network	2D vessel structure	2D structure and function	2D structure and function
Visualized portion	choroid	retina [†]	choroid	retina	choroid

Table 1. Comparison between S-OCA and other angiography methods. D-OCT, Doppler OCT; CIP, choroidal intensity projection. [†] Some Doppler OCT systems and D-OCA are used to investigate the choroid [28, 29].

S-OCA employs the low-scattering property of choroidal vessels. On the other hand, another type of OCA, referred to as D-OCA, uses a Doppler OCT signal as the contrast origin of the vessels. According to the difference between the contrast mechanisms, we can summarize that D-OCA is used to visualize the 3D distribution of blood flow in the retina and the choroid, while S-OCA is used to visualize the 3D structure of the blood vessels in the choroids as summarized in Table 1. D-OCA uses a phase-sensitive Doppler OCT scheme, hence, the phase stability of the OCT system is mandatory, while it is not required for S-OCA.

Lee *et al.* demonstrated the intensity projection of choroids [49]. This projection is a simple, fast, and very robust visualization method for the fine structures of the choroidal vessels, however, it has poorer depth resolution than S-OCA because of its depth-integration nature. In contrast to this projection method, S-OCA enables 3D volume rendering visualization of the choroidal vessels (see section 4.4.2).

FA and ICGA are commonly used for performing angiography in clinics. These methods are safe in most cases; however, some severe adverse reactions have also been reported [23, 24], while OCA and Doppler OCT are perfectly noninvasive techniques. FA and ICGA yield 2D en face images of the human fundus. Although FA and ICGA mainly yield retinal and choroidal angiograms, respectively, their depth resolutions are still poor. The depth resolutions of OCA and Doppler OCT are a great advantage when compared with these two angiograms.

In contrast to the higher depth resolutions of the optical coherence methods, FA and ICGA provide functional information about the retina and choroids, including leakage and metabolism in the fundus. Hence FA/ICGA and coherence-domain angiographic methods are complementary techniques.

4.4.2. S-OCA and intensity inverted volume

It might be considered that a simple intensity-inverted volume of the choroid can provide a 3D visualization of choroidal vessels similar to that provided by S-OCA. To show the advantages of S-OCA, a comparison of S-OCA and the choroidal part of intensity-inverted OCT is shown in Fig. 11. It was found that S-OCA was successfully used to extract the choroidal vasculature and

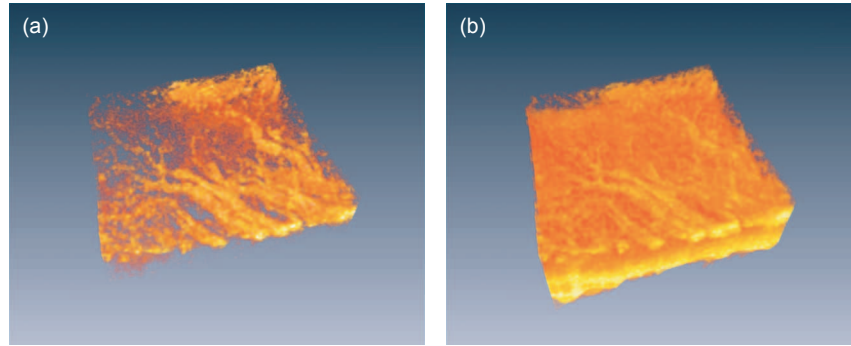


Fig. 11. Comparison between (a) S-OCA and (b) the corresponding intensity-inverted volume.

reject the signals from other regions, while the simple inverted volume contained signals not only from the choroidal vessels but also from the choroid and sclera. Hence, the 3D visibility of the vasculature of a simple inverted volume is insufficient. This difference evidently influences the clinical readabilities of these two 3D images.

5. Conclusions

We demonstrated the *in vivo* imaging of the human posterior eye by using 1- μm SS-OCT. This SS-OCT has a measurement speed of 28,000 A-lines/s and a depth resolution of 10 μm in tissue, and the system sensitivity was measured to be 99.3 dB. A high-speed envelope detection method and adaptive Wiener filter were employed to cancel the uneven shape of a light source spectrum and undesirable spectrum modulation. An automatic dispersion compensation algorithm and morphological imaging filter were introduced to enhance the contrast and clinical readability of the OCT images. A fast fundus preview method for 3D assessment was also presented. The *in vivo* human retina and choroid, as well as the sclera, were visualized by using this SS-OCT.

An OCT intensity-based segmentation algorithm, S-OCA, was developed for the 3D visualization of choroidal vessels. This algorithm revealed the 3D structures of the choroidal vasculature of the *in vivo* human macula and optic nerve head and provided an intuitive and comprehensive understanding of the vasculatures.

Acknowledgements

Youngjoo Hong is a guest student at the University of Tsukuba from Korea Advanced Institute of Science and Technology. Technical contributions from Yasuaki Hori and Yoshifumi Nakamura have been gratefully acknowledged. We are also thankful to Atsushi Sakamoto of Kyoto University Hospital, Rika Homma of Gunma University Hospital, and the OCT group members from TOPCON Corporation for their worthwhile discussions. The specifications of HSL-1000 ver. 1.0 shown in Fig. 2 were provided by Santec Corporation. It should be noted that this is a prototype version of HSL-1000 and has different spectral properties for ver. 2.0 or later. This research has been partially supported by a Grant-in-Aid for Scientific Research 18360029 from the Japan Society for the Promotion of Science (JSPS), Japan Science and Technology Agency, and the Special Research Project of Nanoscience at the University of Tsukuba. Youngjoo Hong is partially supported by a scholarship from Youi-Giken, and Shuichi Makita is supported by JSPS.